https://doi.org/10.5194/tc-2021-183
Preprint. Discussion started: 17 August 2021

The Cryosphere Discussions

Overestimation and Adjustment of Antarctic Ice Flow Velocity Fields Reconstructed from Historical Satellite Imagery

Rongxing Li[1, 2*], Yuan Cheng[1, 2*], Haotian Cui[1, 2], Menglian Xia[1, 2], Xiaohan Yuan[1, 2], Zhen Li[1, 2], Gang Qiao[1, 2]

[1]Center for Spatial Information Science and Sustainable Development Applications, Tongji University, Shanghai, China
[2]College of Surveying and Geo-Informatics, Tongji University, Shanghai, China

Correspondence to: Rongxing Li (rli@tongji.edu.cn)

Abstract. Antarctic ice velocity maps describe the ice flow dynamics of the ice sheet and are one of the primary components used to estimate the Antarctic mass balance and contribution to global sea level changes. In comparison to velocity maps covering monthly to weekly time spans derived from the images of optical imaging satellites taken in recent decades, historical maps, from before the 1990s, generally cover longer time spans, e.g., over 10 years, due to the scarce spatial and temporal coverage of earlier satellite image data. We found velocity overestimations in such long-term maps that can reach from ~69 m a^{-1} (7-year span) in Totten Glacier, East Antarctica, up to ~930 m a^{-1} (10-year span) in Pine Island, West Antarctica. We propose an innovative Lagrangian velocity-based method for overestimation correction without the use of field observations or additional image data. The method is validated by using a set of "ground truth" velocity maps for Totten Glacier which are produced from high-quality Landsat 8 images from 2013 to 2020. Subsequently, the validated method is applied to a historical velocity map of the David Glacier region from images from 1972–1989 acquired during Landsat 1, 4 and 5 satellite missions. It is demonstrated that velocity overestimations of up to 39 m a^{-1} for David Glacier and 69 m a^{-1} for Totten Glacier can be effectively corrected. Furthermore, temporal acceleration information, e.g., on calving events, is preserved in the corrected velocity maps and can be used for long-term ice flow dynamics analysis. We recommend that overestimations of more than the velocity mapping uncertainty (1σ) be corrected. This velocity overestimation correction method can be applied to the production of regional and ice sheet-wide historical velocity maps from long-term satellite images.

1 Introduction

Ice flow velocity fields on the Antarctic ice sheet (AIS) have been mapped by using SAR and optical satellite images to study ice sheet-wide ice flow dynamics and AIS responses to global climate changes (Rignot et al., 2011a; Gardner et al., 2018; Shen et al., 2018; Greene et al., 2020a). An important direct use of such velocity fields is to estimate the ice discharge from the AIS to the Southern Ocean and perform mass balance analyses using the input–output method (IMBIE, 2012; Gardner et al., 2018; IMBIE, 2018; Shen et al., 2018; Rignot et al., 2019). Any errors in the reconstructed velocity fields can cause uncertainties in

https://doi.org/10.5194/tc-2021-183
Preprint. Discussion started: 17 August 2021

the estimated AIS mass balance and associated contribution to global sea level (GSL) change (Rignot et al., 2011b; Church et al., 2013; DeConto & Pollard, 2016; IPCC, 2019).

The state of the reconstructed velocity fields can be represented by a series of velocity maps that are derived from periodical satellite images. The variations of the available satellite images in both spatial and temporal coverage determine the extent and time span of the velocity maps. While ice sheet-wide annual velocity maps, e.g., in the Inter-mission Time Series of Land Ice Velocity and Elevation (ITS_LIVE) project (Gardner et al., 2018, 2019), have been produced from recent satellite images (Storey et al., 2014; Lillesand, 2015; Li & Roy, 2017; Sabins Jr & James, 2020), regional velocity maps at a seasonal or monthly scale have been generated from optical and SAR images (e.g., Landsat 8 and Sentinel 1; Nakamura et al., 2010; Zhou et al., 2014; Greene et al., 2017, 2018, 2020a). Furthermore, a weekly ice velocity mapping scheme based on multi-mission satellite images was proposed in Altena & Kääb (2017). However, owing to low image quality, large geolocation errors, and low temporal and spatial coverage, satellite images prior to 1990 are generally less available; appropriate images for ice sheet-wide or large regional velocity mapping with a shorter time span (e.g., seasonal or annual), especially from 1960s and 1970s, are scarce. Therefore, earlier velocity maps have been produced with a limited extent and a longer time span. For example, combinations of first-generation film – based ARGON images of 1963 (Ruffner, 1995; Kim, 2004) and early Landsat MSS images of 1970s (Wulder et al., 2019) have been used to create regional velocity maps with a time span ranging from 3 to 15 years (Bindschadler & Scambos, 1991; Bindschadler et al., 1996; Wang et al., 2016; Cheng et al., 2019; Rignot et al., 2019; Wulder et al., 2019), although the unique case of a 1963 velocity map of the Rayner Glacier from two ARGON stereo image pairs has been presented (Li et al., 2017). Such a long time span is problematic when we use the feature matching technique for velocity mapping. Given a velocity (spatial) gradient in a region and an initial velocity at a feature point in the first image, the longer the time span of the second image, the greater the additional distance the feature traverses due to acceleration. Using the tracked feature of the second image for velocity mapping would result in an overestimation. With a 10-year span, an overestimation of ~70 m a^{-1} (or ~10%) was estimated for an area near the grounding line of Totten Glacier (Greene, 2020b); similarly, it may reach as high as ~931 m a^{-1} (or ~36%) in front of the Pine Island ice shelf in the Amundsen Sea sector. Berthier et al. (2003) compensated the overestimations in a Mertz Glacier mapping study with an image span of 11 years by assigning the overestimated velocities to middle points of travelled segments. This technique should have corrected a large portion of the overestimation given the relatively weak spatial velocity gradient along the main trunk of the glacier. Although it has not been brought to further attention in publications, given its nature and magnitude, this velocity overestimation issue should be fully understood and a comprehensive correction method should be developed so that corrected historical velocity maps can be analyzed alongside modern maps to create a long record of cohesive ice flow dynamics. Furthermore, this capability of building a long record of AIS ice flow dynamics is important for estimation of long-term AIS mass balance and prediction of the future GSL contribution (Rignot et al., 2019).

This study is a part of our efforts to develop an ice velocity map of East Antarctica for 1963 to 1989 (Li et al., 2017; Ye et al., 2017; Cheng et al., 2019). In this paper we prove the existence of ice velocity overestimation in long-term historical velocity maps and present an innovative correction method. The proposed correction method is based on the Lagrangian velocity that

https://doi.org/10.5194/tc-2021-183
Preprint. Discussion started: 17 August 2021

can be calculated from the overestimated velocity map itself, and thus does not require any field observations or additional satellite images. We used a set of "ground truth" velocity maps with time spans of 1 to 7 years derived from recent Landsat 8 images of 2013 to 2020 from Totten Glacier, East Antarctica, to validate the correction method. We then applied the validated method to a historical velocity map in the David Glacier region, East Antarctica, which was produced from images from 1972 to 1989 acquired during satellite missions of Landsat 1, 4 and 5. It is proven that the 17-year velocity overestimation can be successfully corrected to within the uncertainty (1σ) of the 1-year map. Furthermore, the velocity change information is preserved after the correction and can be used for long-term ice flow dynamics analysis.

2 Methods

2.1 The velocity overestimation issue

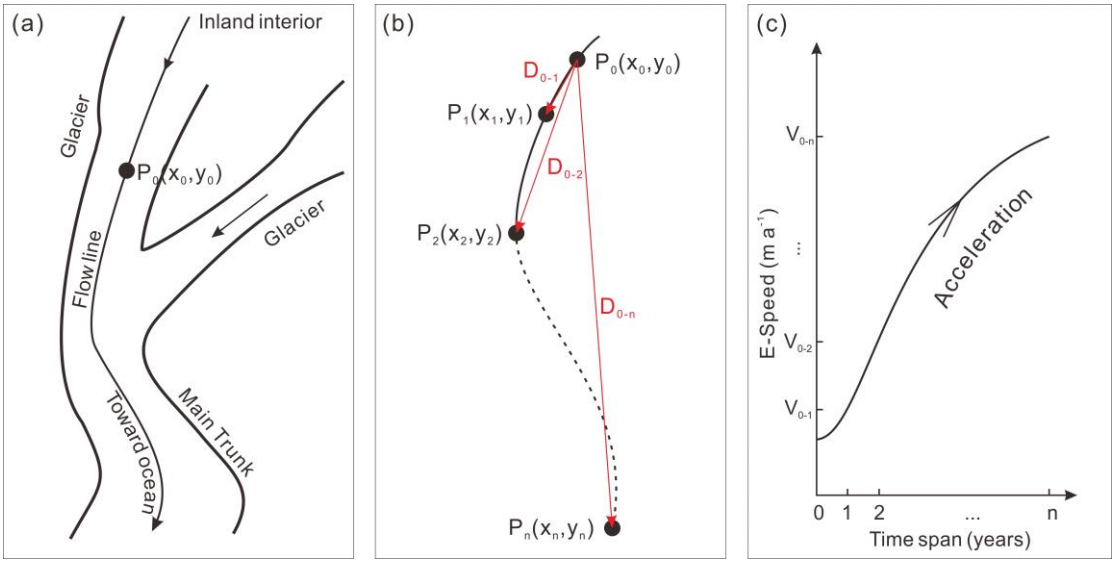

Figure 1: Illustration of acceleration-induced overestimation in a velocity map derived from a satellite image pair with a long time span: (a) schematic scene of accelerated ice flow in a glacier–ice shelf system in AIS; (b) calculation of E-velocities at $P_o(x_o, y_o)$ with an equal increment in time span (1 year); and (c) increase of E-velocity at the same point $P_o(x_o, y_o)$ as the time span increases – the cause of the acceleration-induced velocity overestimation.

We describe an acceleration-induced overestimation using a typical scenario in AIS (Fig. 1a) where ice flow accelerates over descending passages of several glaciers from the inland interior, running through the main trunk, and discharging to the ocean (Bamber et al., 2000; Cuffey & Paterson, 2010; Rignot et al., 2011a). In order to quantify the velocity overestimation, for any point $P_o(x_o, y_o)$ on a glacier (Fig. 1a), we define its velocity in two different frameworks, Eulerian and Lagrangian (Chu & Fan, 2014; Chenillat et al., 2015; Altena & Kääb, 2017). First, the velocity in the Eulerian framework (E-velocity) is defined as $V = D / dt$, the *straight-line* distance (D) divided by the time span (dt). Note that for simplicity in equation derivation and discussion, we interchange a vector with its scalar; thus, velocity and speed are not strictly distinguished in this paper. Hence

https://doi.org/10.5194/tc-2021-183
Preprint. Discussion started: 17 August 2021

a velocity field described by a velocity map is also defined in the Eulerian framework. In reality, the start point of *D* is measured on the first image and end point on the second image; the two images are taken with a time span of *dt* apart (Li, 1998; McGlone, 2013). The reconstructed velocity map is stored as velocity components (V_x, V_y) in the *x* and *y* directions, from which the velocity field can be reconstructed. The velocity, represented by a velocity map, may indicate an "instantaneous" or average velocity depending on the time span *dt* (Cuffey & Paterson, 2010; Rignot et al., 2011a). Second, the velocity in the Lagrangian framework (L-velocity) is defined as $U = S / dt$, the *curved distance traversed along the flow line* (*S*) divided by the time span (*dt*; Altena & Käab, 2017). Given a time span and an initial point $P_o\,(x_o, y_o)$ (Fig. 1a), its L-velocity can be determined by tracking the point using a velocity map (Chu & Fan, 2014; Chenillat et al., 2015). Operations in the Lagrangian framework are often performed to estimate advected ice features (Altena & Käab, 2017) or forecast future events in earth science applications, e.g., mud and debris flow of landslides (Debella-Gilo & Käab, 2013; Feng et al., 2016), ocean currents at different depths (Glenn et al., 2016; van Sebille et al., 2018), and storm center motion of a typhoon or hurricane (Cram et al., 2007; Euler et al., 2019).

Assume that we use a set of *n+1* images ($Image_i$, *i=0, 1, … n*) that are taken with a time interval of 1 year to produce *n* velocity maps, Map_{0-i}, each derived from an image pair ($Image_0$, $Image_i$). The time span of the maps increases from 1 to *n* years. These maps are defined in the Eulerian framework (Fig. 1b). For $P_o(x_o, y_o)$ its location after *i* years, $P_i(x_i, y_i)$, is determined in $Image_i$; its Eulerian distance D_{0-i} is measured using both $Image_0$ and $Image_i$ *(i=1, 2, …n).* Consequently, the E-velocity of an *i*-year span (Δt_{o-i}) at $P_o(x_o, y_o)$ is

$$V_{0-i} = \frac{D_{0-i}}{\Delta t_{0-i}}. \quad (1)$$

As the time span increases at a fixed rate of 1 year, the traversed straight-line distance D_{0-i}, correspondingly E-velocity V_{0-i}, increases rapidly because of the acceleration over the traverse (Fig. 1c). In principle, every V_{0-i} *(i=1, 2, …n)* value represents the velocity at the same point $P_o(x_o, y_o)$ in these *n* velocity maps. In the cases where $Image_i$ were not available and thus Map_{0-i} (*i=1, … n-1*) were not produced, we only had Map_{0-n} with the longest span of *n* years. It is obvious that at $P_o(x_o, y_o)$ its *n*-year velocity V_{0-n} is significantly larger than the 1-year velocity V_{0-1}. In general, we define the velocity overestimation of an *i*-year E-velocity as

$$OE_{0-i} = V_{0-i} - V_{0-1}. \quad (2)$$

Here we use a velocity map of a 1-year span as a baseline. The overestimation becomes more significant as the time span of the velocity maps increases.

2.2 Overestimation correction based on Lagrangian velocity

We propose a method for correction of overestimation in a long-term velocity map based on its Lagrangian velocities. Assume that among all maps Map_{0-i} (*i=1, 2, … n*), the 1-year map Map_{0-1} is "overestimation free", i.e., the magnitude of the overestimation is within the velocity mapping uncertainty (1 σ) and thus, negligible. The velocity field described by this map is used to calculate trajectories of ice mass and L-velocities. The objective is to calculate the overestimation OE_{0-i} in Map_{0-i}

https://doi.org/10.5194/tc-2021-183
Preprint. Discussion started: 17 August 2021

(i=2, … n) so that these maps showing longer spans are corrected using Equation (2) and describe the same velocity field as the 1-year map Map_{0-1}.

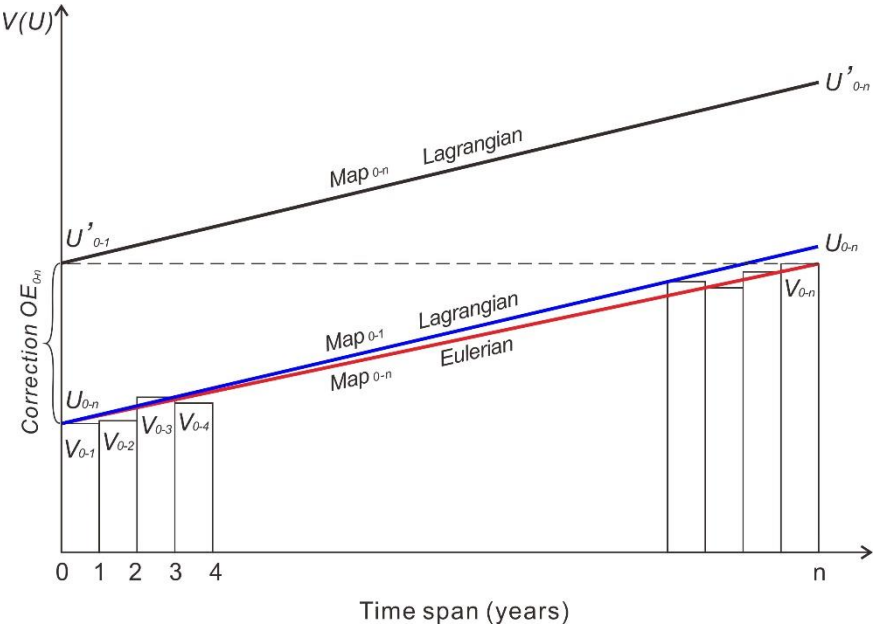

Figure 2: Derivation of equation for overestimation correction using L-velocity

For point $P_o(x_o, y_o)$ in Fig. 1a, the E-velocity V_{0-i} on Map_{0-i} (i=1, 2, … n) is presented by individual bars in Fig. 2. Correspondingly its L-velocity of i-year span can be calculated as (Halliday et al., 2013)

$$U_{0-i} = \frac{S_{0-i}}{\Delta t_{0-i}}, \quad (3)$$

where S_{0-i} is the Lagrangian trajectory (L-trajectory) distance (i=1, 2, … n):

$$S_{0-i} = \int_{t_0}^{t_i} V_{0-1}(P_i)\, dt\ . \quad (4)$$

Within 1 year, the difference between the E-distance and L-distance may be considered within the mapping uncertainty (1 σ): $U_{0-1} \approx V_{0-1}$. Beyond 1 year, the curved trajectory distance is longer than the straight distance ($S_{0-i} \geq D_{0-i}$, see Fig. 1b); thus, we have $U_{0-i} \geq V_{0-i}$ (i=2, 3, … n). An approximation of the increased difference between U_{0-i} and V_{0-i} is presented by the trends of L-velocity (blue line) and E-velocity (red line), which start from the same velocity at U_{0-1} (or V_{0-1}) and reach the maximum difference between U_{0-n} and V_{0-n} at the end (Fig. 2).

***Premise I*:** Within a limited time span the relatively short L-trajectory segment along a flow line is approximately straight, so that the trends of the averaged velocity U_{0-i} in the Lagrangian framework and V_{0-i} in the Eulerian framework (i=1, 2, … n; blue and red lines in Fig. 2) do not deviate significantly from each other, and their maximum difference is limited within a threshold ($U_{0-n} - V_{0-n} \leq k\ \sigma$), where k is a constant and σ is the velocity mapping uncertainty.

https://doi.org/10.5194/tc-2021-183
Preprint. Discussion started: 17 August 2021

In reality the available historical satellite images may only allow us to produce a map, Map_{0-n}, with the longest span of n years and a maximum overestimation of OE_{0-n}. Accordingly Map_{0-n} is used to calculate the L-velocity of the n-year span:

$$U'_{0-i} = \frac{S'_{0-i}}{\Delta t_{0-i}}, \text{ and} \quad (5)$$

$$S'_{0-i} = \int_{t_0}^{t_i} V_{0-n}(P_i)\, dt\,. \quad (6)$$

Hence, the 1-year L-velocity U'_{0-1} from Map_{0-n} is considered to be equal to the n-year E-velocity V_{0-n} within a threshold ($1\ \sigma$; Fig. 2).

***Premise II*:** Within a limited time span, the velocity field described by Map_{0-1} and Map_{0-n} does not change significantly, so that the line between U'_{0-n} and U'_{0-1} (black line in Fig. 2) and that between U_{0-n} and U_{0-1} (blue line in Fig. 2) are approximately parallel to each other. Accordingly, the difference between their simple averaged accelerations is within a threshold ($|\overline{a}(U') - \bar{a}(U)| \leq k' \frac{\sigma}{\Delta t_n}$), where k' is a constant and σ is the velocity mapping uncertainty and

$$\overline{a}(U') = \frac{U'_{0-n} - U'_{0-1}}{\Delta t_n},\ \overline{a}(U) = \frac{U_{0-n} - U_{0-1}}{\Delta t_n}\,. \quad (7)$$

Given the long-term map Map_{0-n} we can calculate the n-year L-velocity U'_{0-n}. Based on *Premise II* we have $U'_{0-n} - U_{0-n} = OE_{0-n}$ (Fig. 2). Furthermore, based on *Premise I* the overestimation can be computed as

$$OE_{0-n} = V_{0-n} - V_{0-1} = U'_{0-n} - V_{0-n}. \quad (8)$$

Consequently, we define the *Correction* as $V_{0-n} - U'_{0-n}$, which adjusts the overestimated E-velocity V_{0-n} of an n-year span to approach the "overestimation-free" E-velocity V_{0-1} of a 1-year span:

$$V_{0-1} = V_{0-n} + Correction + \varepsilon\,, \quad (9)$$

where ε is a residual error that is smaller than a threshold ($k'\ \sigma$). k' is a constant.

2.3 Implementation aspects

Trajectory and L-velocity computation: The computation of the L-trajectory distances S_{0-i} and S'_{0-i} involves the numerical implementation of the integral of the velocity field from $P_o(x_o, y_o)$ to $P_i(x_i, y_i)$ along a flow line on Map_{0-1} and Map_{0-n} using Equations (4) and (6), respectively. We select an area of the velocity map of 2013 of Pine Island Glacier, West Antarctica (Fig. 3a; Gardner et al., 2018), to show the details of integral implementation. The velocity map has a time span of 1 year and a resolution of 240 m. At each grid the velocity is stored according to its components (V_x, V_y). We preprocess each component separately by using a moving window smoothing filter to reduce noise. A 10-year trajectory goes through an ice flow profile from P_0 at 2560 m a^{-1} to P_{10} at 3935 m a^{-1} with an average acceleration of 138 m a^{-2}. As shown in the enlarged area for the annual trajectory from P_2 to P_3 (Fig. 3b), the integral is carried out by accumulation of sub-trajectories (between white dots)

https://doi.org/10.5194/tc-2021-183
Preprint. Discussion started: 17 August 2021

with a monthly increment. The positions are interpolated to the sub-grid level. Finally, we have the result of V_{0-1} = 2560 m a^{-1}, S_{0-10} = 34960 m and U_{0-10} = 3496 m a^{-1}, compared to V_{0-10} = 3491 m a^{-1}. The 10-year overestimation ($V_{0-10} - V_{0-1}$) at P_0 is approximately 931 m a^{-1} (36%). Examples of overestimation correction are given in the Results and Discussion sections.

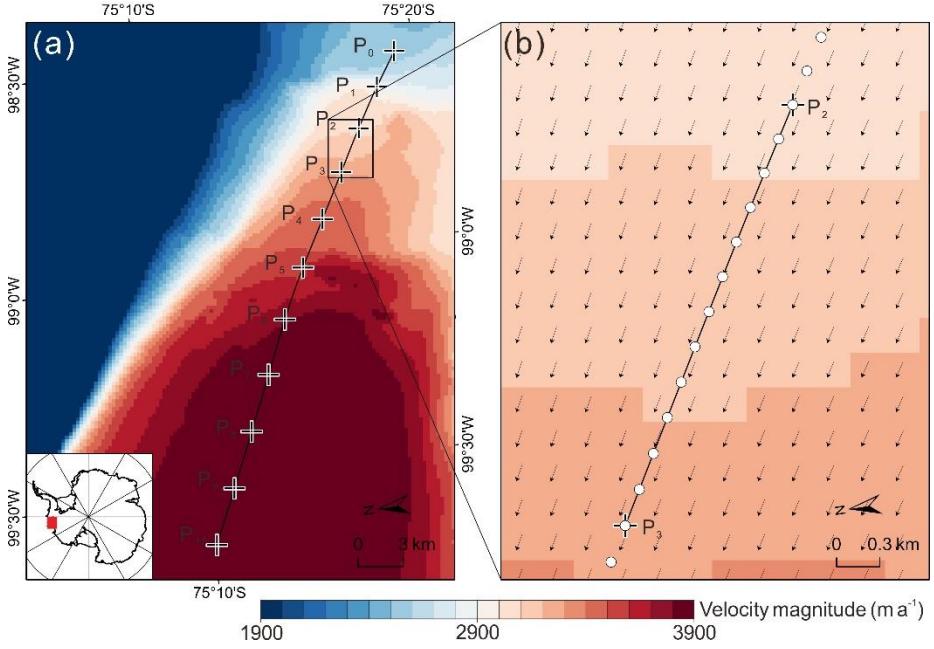

Figure 3: Implementation of numerical integral and L-velocity calculation: (a) 10-year trajectory on a 1-year velocity map of Pine Island Glacier, West Antarctica (Gardner et al., 2018), and (b) numerical integral of the third-year trajectory with a monthly increment.

Denoising and map quality: the quality of the reconstructed velocity field is important for L-trajectory calculation and subsequent overestimation correction. Compared to the above Landsat 8 velocity map, velocity maps derived from historical images may have higher uncertainties due to the low image quality that is inherent in the satellite images of early missions (Kim, 2004; Ye et al., 2017). In some cases, there may be even gaps in the velocity map because image features may not be tracked by using the optical flow or feature matching techniques when ice features disappear through glaciological processes or large advection motion in ice shelf fronts (Scambos et al., 1992; Schenk, 1999; McGlone, 2013). Therefore, preprocessing of the velocity maps should be performed to eliminate outliers; then interpolation may be applied to fill small gaps so that the integral of L-trajectories and the calculation of L-velocities can be realized. Despite the sub-pixel precision of the cross-correlation-based feature matching method, the reconstructed velocity maps may still be subject to a systematic bias called pixel-locking, which results in matched features moving close to integer pixel positions (Shimizu & Okutomi, 2005). This pixel level bias may introduce additional uncertainties to areas of large velocity gradients. The pixel-locking effect can be reduced by using a coarse-to-fine hierarchical feature matching method as demonstrated in the Antarctic and planetary environments (Debella-Gilo & K ääb, 2011; Li et al., 2011; Heid & K ääb, 2012; Li et al., 2017).

https://doi.org/10.5194/tc-2021-183
Preprint. Discussion started: 17 August 2021

The Cryosphere Discussions

Acceleration computation: Given n discrete E-velocities V_{0-i} ($i=1, 2, \ldots n$; Fig. 2), the acceleration can be estimated using a linear regression model. Its least squares (LS) estimation is (Montgomery et al., 2021)

$$a(V) = \frac{n\sum iV_{0-i} - \sum i \sum V_{0-i}}{n\sum i^2 - (\sum i)^2}. \quad (10)$$

On the other hand, this acceleration can also be approximated by an averaged acceleration using the initial and end velocities:

$$\overline{a}(V) = \frac{V_{0-n} - V_{0-1}}{\Delta t}. \quad (11)$$

Here, Δt is n years. The two acceleration estimates can be compared to determine if the averaged acceleration be used in the case that the intermediate velocities V_{0-i} ($i=2, \ldots n-1$) are not available. The red line is then used instead of V_{0-i} ($i=1, 2, \ldots n$; Fig. 2).

3 Results

3.1 Experiment 1: Validation of the correction method at Totten Glacier, East Antarctica

Preparation of validation velocity maps

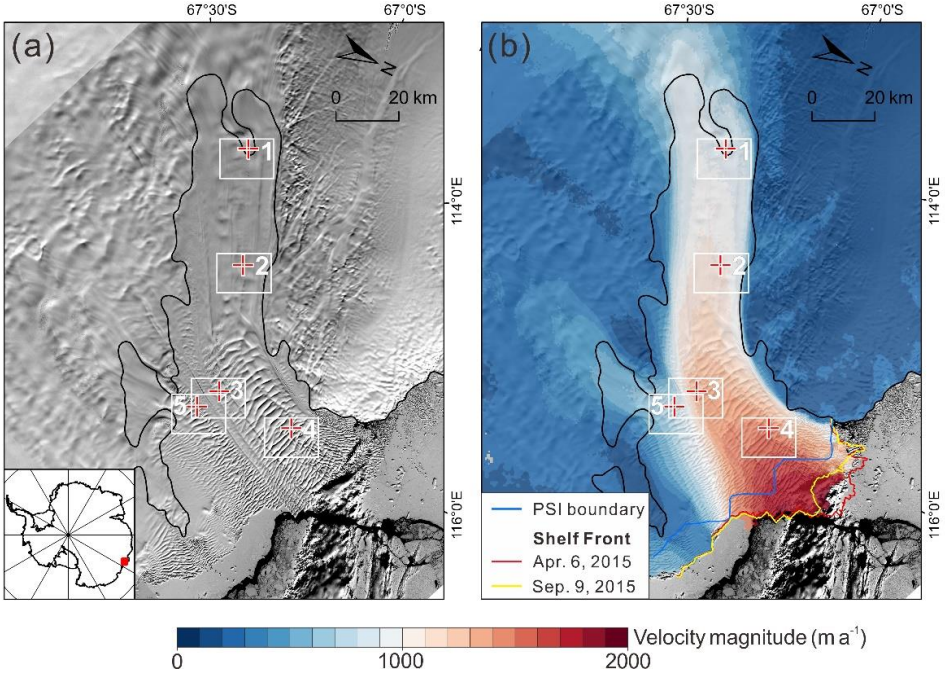

Figure 4: Totten Glacier as an example for the validation of the velocity overestimation correction method: (a) the Totten Glacier region and five areas (white rectangles) selected in different parts of the ice shelf; background is Landsat 8 image of December 3, 2013; black line is grounding line from Rignot et al. (2011c); and (b) velocity map of Totten Glacier of 2013 (Gardner et al., 2018); green and yellow lines are the shelf front of April 5 and September 20, 2015, respectively.

https://doi.org/10.5194/tc-2021-183
Preprint. Discussion started: 17 August 2021

This experiment is designed to validate the proposed velocity overestimation correction method using the velocity data of Totten Glacier (Fig. 4a), which is one of the most active glaciers in East Antarctica and has been experiencing significant mass loss since 1989 (Li et al., 2017; Gardner et al., 2018; Shen et al., 2018). Figure 4b shows an ice flow velocity map of Totten Glacier from 2013 from ITS_LIVE (Gardner et al., 2019). This 240 m resolution velocity map was derived from the 15 m resolution Landsat 8 images with a 1-year span (January to December, 2013). Under the primary forces of gravity, margin shear, basal drag, and others (Bamber et al., 2000; Cuffey & Paterson, 2010; Rignot et al., 2011a), the ice flow accelerates over a path of 130 km along the main trunk at a velocity of ~600 m a^{-1} upstream of the grounding line to ~2300 m a^{-1} at the ice shelf terminus.

In order to validate the velocity overestimation correction method, we need to determine if *Premises I and II* are fulfilled. This further requires us to have E-velocity V_{0-i} from the map series of Map_{0-i} ($i=1, 2, \ldots n$), which are not readily available except the 1-year map of 2013 in Fig. 4b. To avoid lower quality historical velocity maps that may influence the effectiveness of the validation, we use the Landsat 8 images from 2013 to 2020 to produce velocity maps Map_{2013-i} ($i=2014, \ldots 2020$). The validation should also consider velocities of areas with different ice flow dynamics. Thus, we select five areas (white rectangles in Fig. 4) from which to produce smaller maps (~10 km × ~20 km), which contain 7-year trajectories and represent different ice flow dynamic characteristics of the ice shelf, i.e., *Area 1* close to the grounding line, *Areas 2 and 4* along the main trunk, *Area 5* on the tributary flow, and *Area 3* near a suture zone between the main and tributary glaciers.

Using the matching method adapted for ice surface features (Li et al., 2011, 2017), we produced 35 smaller-sized velocity maps Map^{j}_{2013-i} ($i=2014, \ldots 2020; j=1, 2, \ldots 5$) for seven time spans and five areas. Information about the Landsat 8 images used and the acquisition dates are given in Table A1. The "overestimation-free" velocity maps of 1-year $Map^{j}_{2013-2014}$ ($j=1, 2, \ldots 5$) are illustrated in panels 1a–5a of Fig. 5. The corresponding overestimated maps of 7-year $Map^{j}_{2013-2020}$ are shown in panels 1b–5b.

The uncertainty of the maps is estimated from two error sources: the geolocation error of the satellite images σ_{Ref} and the error of feature matching σ_{Match}:

$$\sigma_{Velocity} = \frac{1}{\Delta t}\sqrt{\sigma_{Ref}^2 + \sigma_{Match}^2}, \quad (12)$$

where σ_{Ref} for Landsat 8 images is 18 m (Storey et al., 2014) and σ_{Match} is set to 8 m, ~0.5 pixel (Li et al., 1998 and 2017). Thus, the uncertainty $\sigma_{Velocity}$ is 20 m a^{-1} and 3 m a^{-1} for a 1-year map and a 7-year map, respectively.

In each area, we select an ice feature in the upper stream part in 2013. Its locations in the following 7 years are determined from the satellite images of 2014–2020 using the feature matching method and shown as red dots in the maps (Fig. 5). Correspondingly, we track its annual trajectory locations from the 1-year and 7-year maps using Equations (4) and (6) and plotted them as blue and black dots, respectively, on the maps. Using these trajectories in the Eulerian and Lagrangian frameworks we calculate V^{j}_{2013-i}, U^{j}_{2013-i}, and $U^{'j}_{2013-i}$ and plot them as red, blue, and black curves in panels 1c–5c, respectively.

https://doi.org/10.5194/tc-2021-183
Preprint. Discussion started: 17 August 2021

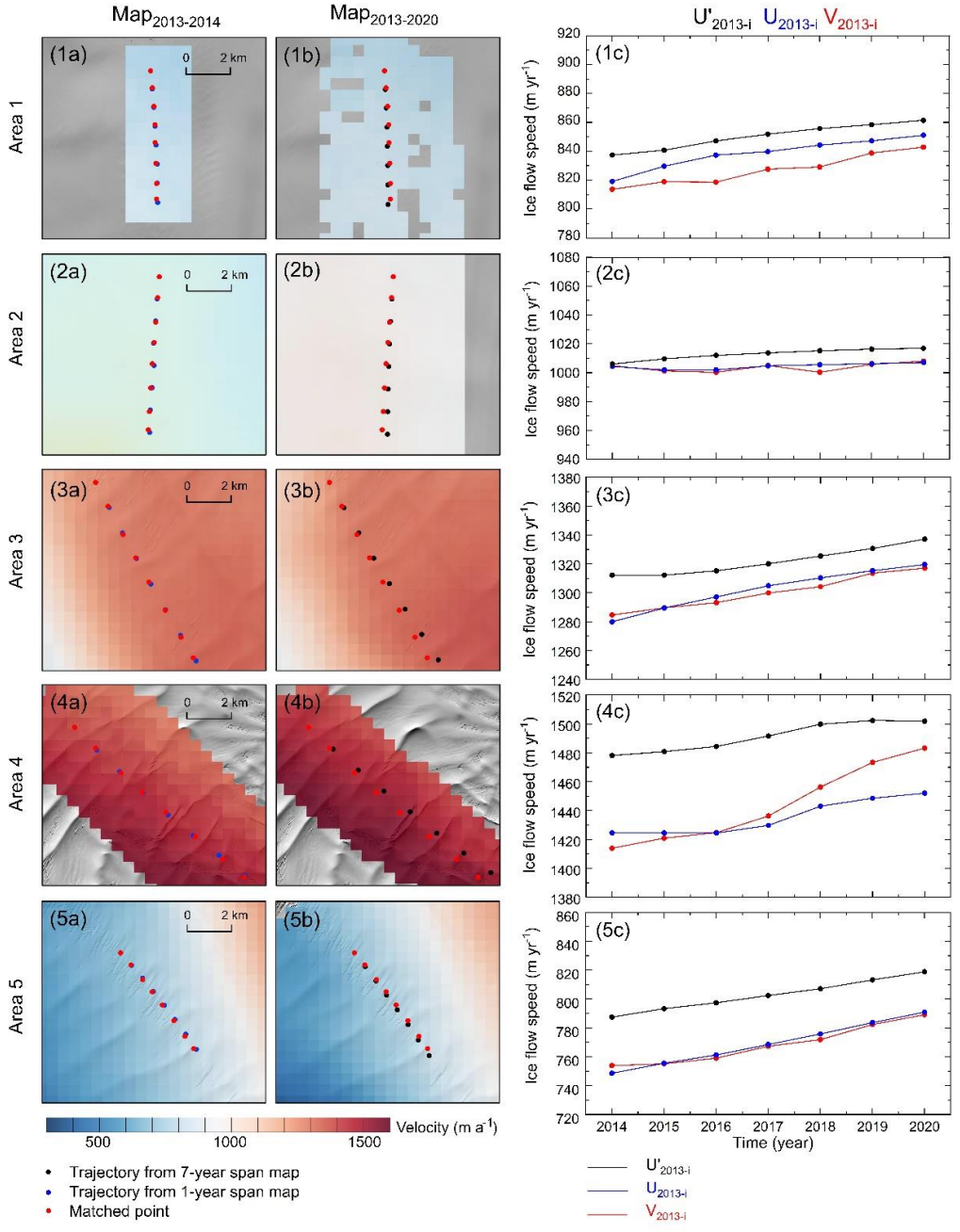

Figure 5: Panels 1a–5a: reconstructed 1-year velocity maps (2013–2014) in five different areas (rectangles in Fig. 4), matched points along a flow line as red dots, and trajectory from these 1-year maps as blue dots; panels 1b–5b: 7-year span velocity maps (2013–2020), matched points as red dots, and trajectory from these 7-year maps as black dots; and panels 1c–5c: velocities of V^{j}_{2013-i}, (red curves), U^{j}_{2013-i} (blue curves), and U'^{j}_{2013-i} (black curves) in five areas.

https://doi.org/10.5194/tc-2021-183
Preprint. Discussion started: 17 August 2021

Validation of Premises I* and *II

In general, the L-velocities from the 1-year map (blue curves in Fig. 5) are mostly faster than and close to the corresponding E-velocities (red curves). To validate *Premise I* we further examine the L-velocity $U^{j}_{2013-2020}$ and E-velocity $V^{j}_{2013-2020}$ (j=*1, 2, … 5*) of the 7-year span, i.e., differences between the end points of blue and red curves in all five areas (panels 1c–5c of Fig. 5). They are less than or equal to 8 m a^{-1} ($(U\text{-}V)_{2013–2020}$ in Table 1), except -31 m a^{-1} in *Area 4*, which was influenced by a calving event in 2015 as mentioned in the Discussion section. The averaged difference of all five areas is -4 ± 16 m a^{-1}, that is, within 20 m a^{-1}, the uncertainty ($1\,\sigma$) of the 1-year velocity map (2013–2014) that is considered "overestimation free". Consequently, the conditions in *Premise I* are met.

For each *Area j* we calculated a least squares acceleration estimate $\boldsymbol{a}$ ($U^{'j}_{2013-i}$) of the 7-year L-velocity $U^{'j}_{2013-i}$ (black curves in panels 1c–5c of Fig. 5) over all years (i=*2013, 2014, … 2020*) using Equations (10); then we calculated an average acceleration $\overline{\boldsymbol{a}}\left(U^{'j}_{2013,2020}\right)$ using Equation (11) based only on the velocities of the beginning and end years (2013 and 2020). In all five areas their differences (Table A2) are less than 1.3 m a^{-2} which is less than 3 m a^{-2}, the acceleration uncertainty estimated from the velocity uncertainty of 20 m a^{-1} ($1\,\sigma$) of the 1-year velocity map of 2013–2014. That means that within the uncertainty of the 1-year velocity map we can substitute the more rigid LS acceleration $\boldsymbol{a}$ represented by a black curve in Fig. 5 with the average acceleration $\overline{\boldsymbol{a}}$ estimated from the straight line between the beginning and end velocities. Similarly, the differences between accelerations $\boldsymbol{a}$ and $\overline{\boldsymbol{a}}$ of the 1-year L-velocity U^{j}_{2013-i} in all five areas (Table A2) are also less than 1.5 m a^{-2}. Within the uncertainty of the 1-year velocity map we can then substitute $\boldsymbol{a}$ (blue curve in Fig. 5) with $\overline{\boldsymbol{a}}$ (straight line) for the 1-year L-velocity U^{j}_{2013-i}.

Validation of *Premise II* requires us to examine the accelerations represented by the 7-year L-velocity $U^{'j}_{2013-i}$ (black curves in Fig. 5) and the 1-year L-velocity U^{j}_{2013-i} (blue curves). The apparent parallelity of the black and blue curves in all five areas shows that the velocity trend in the Lagrangian framework has not changed significantly over the 7 years. This is further quantified by the differences between the averaged 7-year and 1-year accelerations $\overline{\boldsymbol{a}}\left(\boldsymbol{U}'\right)-\overline{\boldsymbol{a}}\left(\boldsymbol{U}\right)$ in Table 1. The differences are within ± 2.1 m a^{-2} in all five areas, with an overall difference of -0.8 ± 1.3 m a^{-2}, which are all within 3 m a^{-2}, the acceleration uncertainty estimated from the velocity uncertainty of the 1-year velocity map (2013–2014). Thus, the conditions in *Premise II* are also fulfilled.

https://doi.org/10.5194/tc-2021-183
Preprint. Discussion started: 17 August 2021

The Cryosphere Discussions

Table 1. Velocity and acceleration in Eulerian and Lagrangian frameworks used for validation of the overestimation correction method.

Area *j*	*Actual E-velocity and OE*			*Premise I*		*Premise II*			*Overestimation correction*			
	$V_{2013–2014}$ (m a^{-1})	$V_{2013–2020}$ (m a^{-1})	OE_{Actual} (m a^{-1})	$U_{2013–2020}$ (m a^{-1})	$(U\text{-}V)_{2013–2020}$ (m a^{-1})	$\bar{a}\left(U'\right)$ (m a^{-2})	$\bar{a}\left(U\right)$ (m a^{-2})	$\bar{a}\left(U'\right)-\bar{a}\left(U\right)$ (m a^{-2})	$U'_{2013–2020}$ (m a^{-1})	*Correction* (m a^{-1})	$V_{Corrected}$ (m a^{-1})	ε (m a^{-1})
1	814	843	29	851	8	3.4	4.6	-1.2	861	-18	825	11
2	1005	1008	3	1007	-1	1.6	0.4	1.2	1017	-9	999	-6
3	1285	1317	32	1320	3	3.6	5.7	-2.1	1337	-20	1297	12
4	1414	1483	69	1452	-31	3.4	3.9	-0.5	1502	-19	1464	50
5	754	789	35	791	2	4.5	6.0	-1.5	819	-30	759	5
MEAN	1054	1088	34	1084	-4	3.3	4.1	-0.8	1107	-19	1069	14
STD	289	302	24	290	16	1.1	2.3	1.3	300	7	304	21

Overestimation correction

As shown in the first part of Table 1, we compare the overestimated E-velocity $V_{2013–2020}$ in the 7-year $Map_{2013–2020}$ with $V_{2013–2014}$ in the 1-year $Map_{2013–2014}$. Their differences make the actual overestimation OE_{Actual} in five areas, which then result in an aggregated overestimation of 34 ± 24 m a^{-1}. The mean overestimation of 34 m a^{-1} with a range from 3 to 69 m a^{-1} is significant in comparison to the uncertainty of 20 m a^{-1} of the 1-year $Map_{2013–2014}$. Thus, the overestimation should be corrected. It should be noted that a higher overestimation is expected for historical velocity maps of longer time spans, e.g., 10–15 years.

Using our correction method in Equation (9), we estimated the *Correction* term ($V_{2013–2020} - U'_{2013–2020}$) and applied it to the overestimated $V_{2013–2020}$ (Table 1). After the overestimation correction, the corrected velocity $V_{Corrected}$ from the 7-year $V_{2013–2020}$ is agreeable to the 1-year $V_{2013–2014}$ within an average difference of 15 m a^{-1}, which is less than the 20 m a^{-1} uncertainty of $Map_{2013–2014}$.

3.2 Experiment 2: Velocity overestimation correction in the David Glacier region, East Antarctica

This experiment demonstrates the applicability of the introduced method to correct the overestimation in historical velocity maps derived from long-term images. We produced a velocity map of the David Glacier on the Scott Coast, East Antarctica, from 64 Landsat images collected from 1972 to 1989 (Table A3). The image pairs used for velocity mapping have mainly four time spans, namely 1, 15, 16 and 17 years, with their footprints illustrated in Fig. 7a. The Landsat images were first orthorectified using ground control points (GCPs), which were selected at outcrops, blue ice, and ice rises (Ye et al., 2017). Then the velocity field was reconstructed in three steps: a) measurement of a set of manually selected seed points for representing the initial structural velocity information in stationary, low velocity, and dynamic flow areas; b) velocity point generation by the ice surface feature-based matching method controlled by a triangular irregular network (TIN) model and initiated by the seed points; and c) dense grid matching for generation of the gridded ice velocity field with a mixed time span from 1972 to 1989. This feature and grid image matching method has been developed for surface mapping from optical satellite images in challenging planetary and polar environments, and successfully applied to the reconstruction of the ice velocity

https://doi.org/10.5194/tc-2021-183
Preprint. Discussion started: 17 August 2021

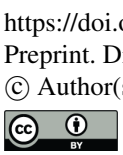

The Cryosphere Discussions
Open Access
EGU

fields in the Rayner and Fimbul ice shelves in East Antarctica from historical optical satellite images of 1963–1987 (Li et al., 2011, 2017). The produced velocity map has a grid spacing of 500 m after a Kriging interpolation from all matched feature and grid points (Fig 7b). The uncertainty (1σ) of the velocity points is 4 m a^{-1}, 31 m a^{-1} and 62 m a^{-1} for time spans of 15–17 years, 1 year (TM), and 1 year (MSS), respectively.

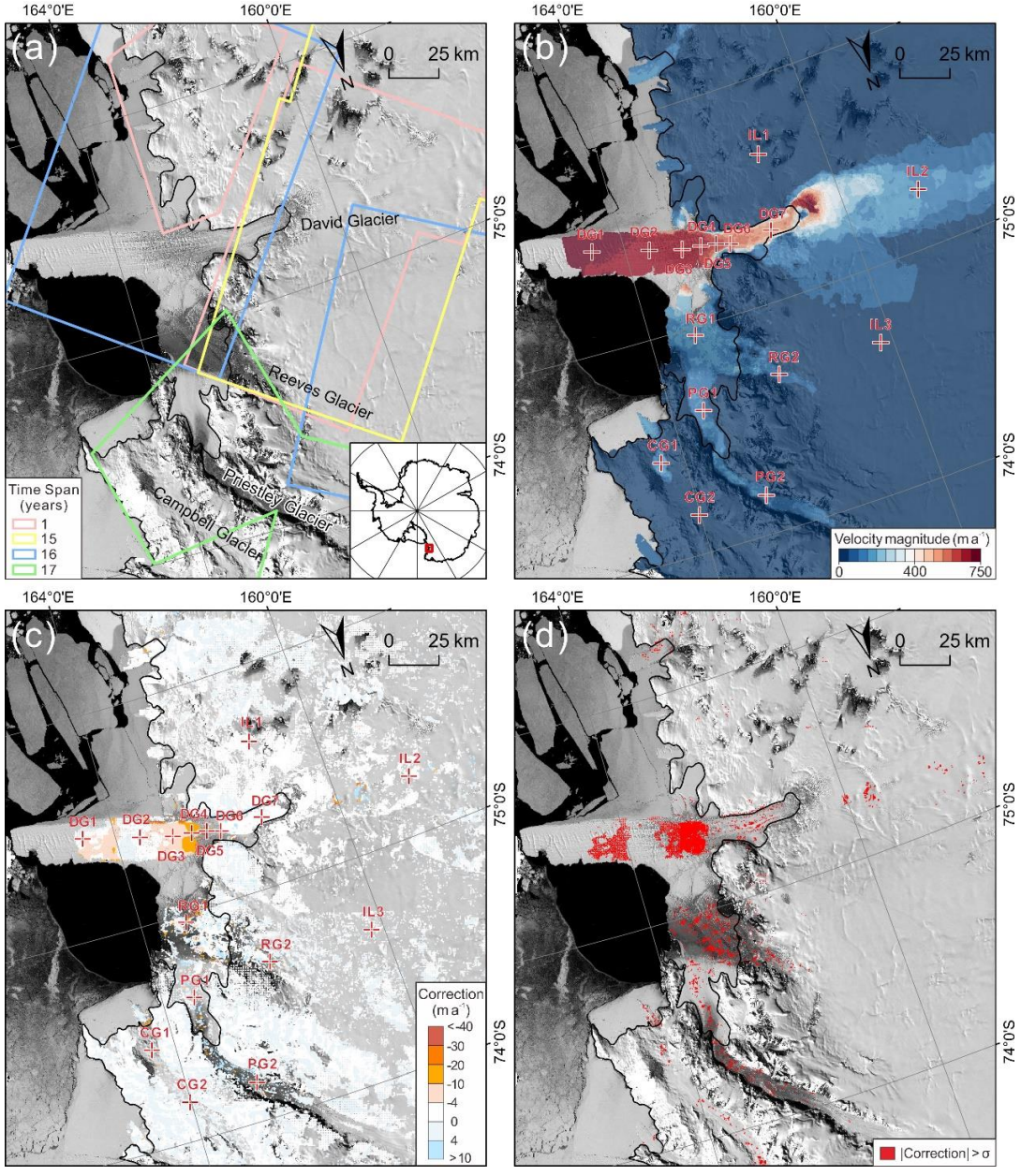

Figure 6: Application of the overestimation correction method to a historical velocity map of 1972–1989 of the David Glacier region, East Antarctica. (a) Footprints and time spans of the Landsat image pairs used for velocity mapping with a background of Landsat Image Mosaic of Antarctica (Bindschadler et al., 2008), (b) produced velocity map of 1972–1989 and selected points for examination

https://doi.org/10.5194/tc-2021-183
Preprint. Discussion started: 17 August 2021

of velocity overestimation and correction, (c) overestimation values of all velocity points generated using the image feature matching technique, and (d) velocity points with OE ≥ 1σ (red points).

At all velocity points, including 8564 matched feature from the feature matching process and 59783 grid points from the dense grid matching process, we calculated the velocity overestimation (OE) values (Fig. 6c). The OEs are generally low on the grounded ice, mostly within ±4 m a^{-1}, which are less than the mapping uncertainties (1σ) of different time spans (Fig. 6d and Table 2). The higher OEs ranging from ~4 m a^{-1} to ~50 m a^{-1} are on the ice tongue, ice shelves, and glaciers. We selected a total of 16 points from four glaciers and the inland region to examine detailed OEs in different areas of ice flow dynamics (Figs. 6b and 6c). The OEs at three points in the inland region (IL1–IL3) are negligible (Table 2). Points DG1–DG6 along the main trunk of the David Glacier present an increasing trend of OEs from 1 to 4 m a^{-1} on the ice tongue up to 36 m a^{-1} at the ice shelf outlet, as the average Lagrangian acceleration $\overline{\boldsymbol{a}}\,(\boldsymbol{U'})$ increases from 0.1 m a^{-2} to 2.2 m a^{-2}. However, DG7 is located in a relatively steady velocity area, and thus has negligible overestimation. Furthermore, the OE values at the selected points on the smaller glaciers, Reeves Glacier (RG1 and RG2), Priestley Glacier (PG1 and PG2), and Campbell Glacier (CG1 and CG2), range from 0 m a^{-1} to 12 m a^{-1} and are generally greater than those on the grounded ice. At the velocity points where the OEs are greater than or equal to the velocity mapping uncertainties (1σ), the corrected velocities are calculated by applying the overestimation corrections.

Table 2: Ice flow dynamics parameters, computed OEs, and corrected velocities at 16 selected points

ID	Time span (years)	$V_{Original}$ (m a^{-1})	$1\,\sigma$ (m a^{-1})	$\overline{a}\,(U')$ (m a^{-2})	*Correction (-OE)* (m a^{-1})	$V_{Corrected}$ (m a^{-1})
DG1	15.95	717	4	0.2	-4	713
DG2	15.95	692	4	0.1	-1	692
DG3	15.95	679	4	0.3	-5	674
DG4	15.95	665	4	0.8	-12	653
DG5	15.95	634	4	1.4	-22	612
DG6	15.95	572	4	2.2	-36	536
DG7	1.04	524	62	0.0	0	524
RG1	16.96	125	4	0.7	-12	113
RG2	15.18	88	4	0.5	-7	81
PG1	16.96	110	4	0.4	-7	103
PG2	16.96	100	4	0.3	-6	94
CG1	16.96	143	4	0.3	-5	138
CG2	16.96	36	4	0.0	0	36
IL1	1.00	8	31	0.0	0	8
IL2	1.04	168	62	0.0	0	168
IL3	16.16	15	4	0.0	0	15
MEAN	**13.43**	**330**	**13**	**0.5**	**-7**	**323**
STD	**6.18**	**289**	**20**	**0.6**	**10**	**286**

https://doi.org/10.5194/tc-2021-183
Preprint. Discussion started: 17 August 2021

315

Overall, for a historical velocity map of 1972–1989 with time spans from 1 to 17 years in the David Glacier region, the overestimations and corrections mainly occur on the David Glacier and smaller glaciers where accelerations in the spatial domain (not the temporal domain) exist, while those on the grounded ice are non-significant. It is recommended that the overestimations that are greater than or equal to the mapping uncertainties (1σ) be corrected.

320 **4. Discussion**

Area 4 in Experiment 1 is located in a dynamic area of a velocity of ~1400 m a^{-1}, about 30 km from the ice shelf front (Fig. 4). In Fig. 5, different from the four other areas (*Areas 1, 2, 3, and 5*), where the L-velocities are generally faster than E-velocity (panels 1c, 2c, 3c and 5c), the E-velocity in *Area 4* (red curve in panel 4c) exceeded the L-velocity (blue curve) in 2016 and showed a significant acceleration thereafter. This resulted in the largest actual overestimation OE_{Actual} of ~69 m a^{-1} (Table 1),
325 which may be attributed to large shelf front calving occurring during the period between April 6 and September 20, 2015, with an area loss of 136 km^2 (2%; Fig. 4b). However, it appears that the calving event did not significantly reduce the buttressing potential of the ice shelf because the ice shelf front retreat occurred outside of the passive shelf-ice (PSI) boundary (light blue line in Fig. 4b; Fürst et al., 2016); the other four areas are located farther away, inland, and away from the PSI boundary and thus were not influenced as much as in *Area 4*. Therefore, the calving-induced acceleration only occurred in *Area 4*, but not in
330 the four other areas.

Furthermore, this acceleration signature due to the 2015 calving event exists in all E-velocities from 2016 to 2020 in *Area 4* (red curve in panel 4c of Fig. 5), while the L-velocities (blue curve), which are derived from the 1-year map $Map_{2013–2014}$ before 2015, show initial spatial acceleration. Thus, any large difference between the red and blue curves should demonstrate a significant acceleration deviating from its initial pattern. On the other hand, the effect of the calving-induced acceleration is
335 averaged out in the 7-year L-velocity (black curve in panel 4c of Fig. 5) over 7 years. The black and blue curves are generally parallel and their average accelerations $\bar{a}$ differ only by -0.5 m a^{-2} (Table 1). Hence, the calculated correction of -19 m a^{-1} in *Area 4* is at a similar level to that in the four other areas and have only adjusted the overestimation caused by the spatial acceleration along the trajectory. The velocity increase due to the temporal acceleration by the calving event remains in the adjusted map as a large "residual" of 50 m a^{-1}, which can serve as a signature to study the relationship between calving activities
340 and ice flow dynamics. This shows the stability of the introduced method of velocity overestimation correction and its capability of preserving temporal velocity change signatures that may be attributed to both local events (e.g., calving) and global influences (e.g., intrusion of the warm modified Circumpolar Deep Water; Roberts et al., 2011; Gwyther et al., 2014; Greene et al., 2017).

This paper presents a general method to correct overestimations in velocity fields reconstructed from satellite images with long
345 time spans. For ice sheet – wide and large regional scale velocity mapping, we expect that overestimations in majority of the low velocity regions on grounded ice are small and may not need to be corrected. However, the method is especially important

https://doi.org/10.5194/tc-2021-183
Preprint. Discussion started: 17 August 2021

for velocity mapping in Antarctic glacier – ice shelf systems and may be also applicable to outlet glaciers of the Greenland Ice Sheet, where the velocity spatial gradient is strong and temporal image coverage may not be ideal.

The main focus of this study is to develop an overestimation correction method that can be used to map earlier velocity fields in Antarctica, which can be used along with recent velocity fields derived from newer satellite observations for long-term ice flow dynamics analysis and mass balance estimation. However, the method may also provide a tool to reconfirm or reexamine outcomes of past studies that detected velocity changes of the ice sheets. The impact of the overestimation correction on such velocity changes may be significant in glaciers with high spatial velocity gradients and long image time spans.

5 Conclusions

Velocity overestimation exists in Antarctic ice flow velocity maps produced from optical satellite images of long time spans. Such overestimations are inevitable for historical velocity maps due to the poor availability of earlier satellite images in Antarctica, especially before 1990. The results in this study show that the overestimations can reach up to ~69 m a^{-1} in the Totten Glacier, East Antarctica, over a 7-year span and ~931 m a^{-1} in the Pine Island Glacier, West Antarctica, over a 10-year span. The overestimated historical velocity maps should be adjusted before they are combined with recent velocity maps to build a long-term record for monitoring and forecasting the Antarctic ice flow dynamics and impact of global climate changes on the ice sheet. We used a set of "ground truth" velocity maps in the Totten Glacier produced from Landsat 8 images of 2013 to 2020 to validate the proposed innovative method for velocity overestimation correction. Based on the validated method, we successfully corrected the overestimations of a velocity map of 1972–1989 with time spans from 1 to 17 years in the David Glacier region, East Antarctica. In summary we draw the following conclusions.

1) The proposed Lagrangian velocity-based method is effective and easy to implement because the overestimation corrections are calculated by using the long-term velocity map itself only, without field observations or additional image data.
2) The premises of the correction method are validated by using a set of "ground truth" velocity maps developed from high-quality Landsat 8 images from 2013 to 2020 to show the rigidity of the method. The velocity overestimations of a 7-year span are proven to be corrected effectively to within the uncertainty (1σ) of the 1-year map.
3) The validated correction method is then successfully applied to correct overestimations in a historical velocity map of 1972–1989 with time spans from 1 to 17 years.
4) It is proven that ice velocity change information of temporal acceleration events, e.g., caused by shelf front calving, is preserved after the correction and can be used for long-term ice flow dynamics analysis.

It is recommended that OE values be computed for long-term historical velocity maps and corrections be made when OEs are more than the velocity uncertainty (1σ). This velocity overestimation correction method can be applied to adjust velocity fields for the production of regional and ice sheet-wide historical velocity maps from long-term satellite images before 1990s.

https://doi.org/10.5194/tc-2021-183
Preprint. Discussion started: 17 August 2021

Author contributions. RL led the study and developed the overestimation correction model. YC, MX, XY and ZL carried out velocity mapping. HC performed programing. RL, YC and GQ were involved in data analysis and presentation.

Competing interests. The authors declare that they have no conflict of interest.

Acknowledgements. This research has been supported by the National Science Foundation of China (grant no. 41730102) and Polar Expedition Office of the State Oceanic Administration of China. The authors would like to thank the United States Geological Survey (USGS) for the Landsat images.

https://doi.org/10.5194/tc-2021-183
Preprint. Discussion started: 17 August 2021

References

Altena, B., and Kääb, A.: Weekly Glacier Flow Estimation from Dense Satellite Time Series Using Adapted Optical Flow Technology, Front. Earth. SCI., 5(53), http://doi.org/10.3389/feart.2017.00053, 2017.

Bamber, J. L., Vaughan, D. G., and Joughin, I.: Widespread complex flow in the interior of the Antarctic ice sheet, Science, 287(5456), 1248-1250, http://doi.org/10.1126/science.287.5456.1248, 2000.

Berthier, E., Raup, B., and Scambos, T.: New velocity map and mass-balance estimate of Mertz Glacier, East Antarctica, derived from Landsat sequential imagery, J. Glaciol., 49(167), 503-511, http://doi.org/10.3189/172756503781830377, 2003.

Bindschadler, R., Vornberger, P., Blankenship, D., Scambos, T., and Jacobel, R.: Surface velocity and mass balance of Ice Streams D and E, West Antarctica, J. Glaciol., 42(142), 461-475, http://doi.org/10.3189/S0022143000003452, 1996.

Bindschadler, R., Vornberger, P., Fleming, A., Fox, A., Mullins, J., Binnie, D., Paulsen, S. J., Granneman, B., and Gorodetzky, D.: The Landsat Image Mosaic of Antarctica, Remote Sens. Environ., 112(12), 4214-4226, http://doi.org/10.1016/j.rse.2008.07.006, 2008.

Bindschadler, R. A., and Scambos, T. A.: Satellite-Image-Derived Velocity Field of an Antarctic Ice Stream, Science, 252(5003), 242-246, http://doi.org/10.1126/science.252.5003.242, 1991.

Cheng, Y., Li, X., Qiao, G., Ye, W., Huang, Y., Li, Y., Wang, K., Tian, Y., Tong, X., and Li, R.: Ice flow velocity mapping of East Antarctica from 1963 to 1989, International Society for Photogrammetry and Remote Sensing (ISPRS) Geospatial Week 2019, Enschede, the Netherlands, 10 – 14 June 2019, XLII-2/W13, 2019.

Chenillat, F., Blanke, B., Grima, N., Franks, P. J. S., Capet, X., and Riviere, P.: Quantifying tracer dynamics in moving fluids: a combined Eulerian-Lagrangian approach, Front. Earth Sci., 3(43), http://doi.org/10.3389/fenvs.2015.00043, 2015.

Chu, P. C., and Fan, C.: Accuracy Progressive Calculation of Lagrangian Trajectories from a Gridded Velocity Field, J. Atmos. Ocean. Tech., 31(7), 1615-1627, http://doi.org/10.1175/JTECH-D-13-00204.1, 2014.

Church, J. A., Monselesan, D., Gregory, J. M., and Marzeion, B.: Evaluating the ability of process based models to project sea-level change, Environ. Res. Lett., 8(1), http://doi.org/10.1088/1748-9326/8/1/014051, 2013.

Cram, T. A., Persing, J., Montgomery, M. T., and Braun, S. A.: A lagrangian trajectory view on transport and mixing processes between the eye, eyewall, and environment using a high-resolution simulation of Hurricane Bonnie (1998), J. Atmos. Sci., 64(6), 1835-1856, http://doi.org/10.1175/JAS3921.1, 2007.

Cuffey, K. M., and Paterson, W. S. B.: The physics of glaciers, Fourth edition, Academic Press, Burlington, USA, 2010.

Debella-Gilo, M., and Kääb, A.: Sub-pixel precision image matching for measuring surface displacements on mass movements using normalized cross-correlation, Remote Sens. Environ., 115(1), 130-142, http://doi.org/10.1016/j.rse.2010.08.012, 2011.

Debella-Gilo, M., and Kääb, A.:Monitoring slow-moving landslides using spatially adaptive least squares image matching, in Landslide Science and Practice, Springer, Berlin, Heidelberg.

DeConto, R. M., and Pollard, D.: Contribution of Antarctica to past and future sea-level rise, Nature, 531(7596), 591-597, http://doi.org/10.1038/nature17145, 2016.

Euler, C., Riemer, M., Kremer, T., and Schömer, E.: Lagrangian Description of Air Masses Associated with Latent Heat Release in Tropical Storm Karl (2016) during Extratropical Transition, Mon. Weather Rev., 147(7), 2657-2676, http://doi.org/10.1175/MWR-D-18-0422.1, 2019.

Feng, T., Mi, H., Scaioni, M., Qiao, G., Lu, P., Wang, W., Tong, X., and Li, R.: Measurement of Surface Changes in a Scaled-Down Landslide Model Using High-Speed Stereo Image Sequences, Photogramm. Eng. Rem. S., 82(7), 547-557, http://doi.org/10.14358/PERS.82.7.547, 2016.

Fürst, J. J., Durand, G., Gillet-Chaulet, F., Tavard, L., Rankl, M., Braun, M., and Gagliardini, O.: The safety band of Antarctic ice shelves, Nat. Clim. Change, 6(5), 479-482, http://doi.org/10.1038/nclimate2912, 2016.

Gardner, A. S., Moholdt, G., Scambos, T., Fahnstock, M., Ligtenberg, S., van den Broeke, M., and Nilsson, J.: Increased West Antarctic and unchanged East Antarctic ice discharge over the last 7 years, The Cryosphere, 12(2), 521-547, http://doi.org/10.5194/tc-12-521-2018, 2018.

Gardner, A. S., Fahnestock, M. A., and Scambos, T. A.: ITS_LIVE Regional Glacier and Ice Sheet Surface Velocities, National Snow and Ice Data Center, pp., 2019.

Glenn, S. M., Miles, T. N., Serokal, G. N., Xu, Y., Forney, R. K., Yu, F., Roarty, H., Schofield, O., and Kohut, J.: Stratified coastal ocean interactions with tropical cyclones, Nat. Commun., 7(10887), http://doi.org/10.1038/ncomms10887, 2016.

Greene, C. A., Blankenship, D. D., Gwyther, D. E., Silvano, A., and van Wijk, E.: Wind causes Totten Ice Shelf melt and acceleration, Science Advances, 3(11), e1701681, http://doi.org/10.1126/sciadv.1701681, 2017.

Greene, C. A., Young, D. A., Gwyther, D. E., Galton-Fenzi, B. K., and Blankenship, D. D.: Seasonal dynamics of Totten Ice Shelf controlled by sea ice buttressing, Cryosphere, 12(9), 2869-2882, http://doi.org/10.5194/tc-12-2869-2018, 2018.

Greene, C. A., Gardner, A. S., and Andrews, L. C.: Detecting seasonal ice dynamics in satellite images, The Cryosphere, 14(12), 4365-4378, http://doi.org/10.5194/tc-14-4365-2020, 2020a.

Greene, C. A.: Personal communication, Comments on a manuscript,2020b.

Gwyther, D. E., Galton-Fenzi, B. K., Hunter, J. R., and Roberts, J. L.: Simulated melt rates for the Totten and Dalton ice shelves, Ocean Sci., 10(3), 267-279, http://doi.org/10.5194/os-10-267-2014, 2014.

Halliday, D., Resnick, R., and Walker, J.: Fundamentals of physics, John Wiley & Sons, 2013.

Heid, T., and Kääb, A.: Evaluation of existing image matching methods for deriving glacier surface displacements globally from optical satellite imagery, Remote Sens. Environ., 118(339-355, http://doi.org/10.1016/j.rse.2011.11.024, 2012.

IMBIE.: A Reconciled Estimate of Ice-Sheet Mass Balance, Science, 338(6111), 1183-1189, http://doi.org/10.1126/science.1228102, 2012.

IMBIE.: Mass balance of the Antarctic Ice Sheet from 1992 to 2017, Nature, 558(7709), 219-222, http://doi.org/10.1038/s41586-018-0179-y, 2018.

IPCC.: The Ocean and Cryosphere in a Changing Climate: A Special Report of the Intergovernmental Panel on Climate Change, Working Group II Technical Support Unit, 756 pp., 2019.

Kim, K.: Satellite mapping and automated feature extraction: geographic information system-based change detection of the

https://doi.org/10.5194/tc-2021-183
Preprint. Discussion started: 17 August 2021

Antarctic coast, Doctoral dissertation, The Ohio State University, Columbus, Ohio, 171 pp., 2004.

Li, J., and Roy, D. P.: A Global Analysis of Sentinel-2A, Sentinel-2B and Landsat-8 Data Revisit Intervals and Implications for Terrestrial Monitoring, Remote Sens.-Basel, 9(9029), http://doi.org/10.3390/rs9090902, 2017.

Li, R.: Potential of high-resolution satellite imagery for national mapping products, Photogramm. Eng. Rem. S., 64(12), 1165-1169,1998.

Li, R., Hwangbo, J., Chen, Y., and Di, K.: Rigorous Photogrammetric Processing of HiRISE Stereo Imagery for Mars Topographic Mapping, IEEE T. Geosci. Remote, 49(7), 2558-2572, http://doi.org/10.1109/TGRS.2011.2107522, 2011.

Li, R., Ye, W., Qiao, G., Tong, X., Liu, S., Kong, F., and Ma, X.: A New Analytical Method for Estimating Antarctic Ice Flow in the 1960s From Historical Optical Satellite Imagery, in:The International Archives of the Photogrammetry, Remote Sensing and Spatial Information Sciences, 2771-2785, 2017.

Lillesand, T. R. W. K.: Remote sensing and image interpretation, 7th Edition ed., John Wiley & Sons, 2015.

McGlone, J. C.: Manual of Photogrammetry, Sixth Edition, ASPRS Publications, Maryland, MD, USA, 2013.

Montgomery, D. C., Peck, E. A., and Vining, G. G.: Introduction to Linear Regression Analysis, 6th Edition ed., John Wiley & Sons, 2021.

Nakamura, K., Doi, K., and Shibuya, K.: Fluctuations in the flow velocity of the Antarctic Shirase Glacier over an 11-year period, POLAR SCIENCE, 4(3), 443-455, http://doi.org/10.1016/j.polar.2010.04.010, 2010.

Rignot, E., Mouginot, J., and Scheuchl, B.: Ice Flow of the Antarctic Ice Sheet, Science, 333(6048), 1427-1430,2011a.

Rignot, E., Velicogna, I., van den Broeke, M. R., Monaghan, A., and Lenaerts, J.: Acceleration of the contribution of the Greenland and Antarctic ice sheets to sea level rise, Geophys. Res. Lett., 38(http://doi.org/10.1029/2011GL046583, 2011b.

Rignot, E., Mouginot, J., and Scheuchl, B.: Antarctic grounding line mapping from differential satellite radar interferometry, Geophys. Res. Lett., 38(L10504), http://doi.org/10.1029/2011GL047109, 2011c.

Rignot, E., Mouginot, J., Scheuchl, B., van den Broeke, M., van Wessem, M. J., and Morlighem, M.: Four decades of Antarctic Ice Sheet mass balance from 1979 – 2017, Proc. Natl. Acad. Sci., 116(4), 1095-1103, http://doi.org/10.1073/pnas.1812883116, 2019.

Roberts, J. L., Warner, R. C., Young, D., Wright, A., van Ommen, T. D., Blankenship, D. D., Siegert, M., Young, N. W., Tabacco, I. E., Forieri, A., Passerini, A., Zirizzotti, A., and Frezzotti, M.: Refined broad-scale sub-glacial morphology of Aurora Subglacial Basin, East Antarctica derived by an ice-dynamics-based interpolation scheme, The Cryosphere, 5(3), 551-560, http://doi.org/10.5194/tc-5-551-2011, 2011.

Ruffner, K. C. (1995), CORONA: America's First Satellite Program.

Sabins Jr, F., and James, F. A.: Remote Sensing: Principles, Interpretation, and Applications, Fourth Edition ed., Waveland Press, 2020.

Scambos, T. A., Dutkiewicz, M. J., Wilson, J. C., and Bindschadler, R. A.: Application of image cross-correlation to the measurement of glacier velocity using satellite image data, Remote Sens. Environ., 42(3), 177-186, http://doi.org/10.1016/0034-4257(92)90101-O, 1992.

https://doi.org/10.5194/tc-2021-183
Preprint. Discussion started: 17 August 2021

Schenk, T.: Digital Photogrammetry, TerraScience, 1999.

Shen, Q., Wang, H., Shum, C. K., Jiang, L., Hsu, H. T., and Dong, J.: Recent high-resolution Antarctic ice velocity maps reveal increased mass loss in Wilkes Land, East Antarctica, Sci. Rep.-UK, 8(1), 4477, http://doi.org/10.1038/s41598-018-22765-0, 2018.

Shimizu, M., and Okutomi, M.: Sub-pixel estimation error cancellation on area-based matching, Int. J. Comput. Vision, 63(3), 207-224, http://doi.org/10.1007/s11263-005-6878-5, 2005.

Storey, J., Choate, M., and Lee, K.: Landsat 8 Operational Land Imager On-Orbit Geometric Calibration and Performance, Remote Sens.-Basel, 6(11), 11127-11152, http://doi.org/10.3390/rs61111127, 2014.

van Sebille, E., Griffies, S. M., Abernathey, R., Adams, T. P., Berloff, P., Biastoch, A., Blanke, B., Chassignet, E. P., Cheng, Y., Cotter, C. J., Deleersnijder, E., Doos, K., Drake, H. F., Drijfhout, S., Gary, S. F., Heemink, A. W., Kjellsson, J., Koszalka, I. M., Lange, M., Lique, C., MacGilchrist, G. A., Marsh, R., Adame, C. G. M., McAdam, R., Nencioli, F., Paris, C. B., Piggott, M. D., Polton, J. A., Ruehs, S., Shah, S. H. A. M., Thomas, M. D., Wang, J., Wolfram, P. J., Zanna, L., and Zika, J. D.: Lagrangian ocean analysis: Fundamentals and practices, Ocean Model., 121(49-75, http://doi.org/10.1016/j.ocemod.2017.11.008, 2018.

Wang, S., Liu, H., Yu, B., Zhou, G., and Cheng, X.: Revealing the early ice flow patterns with historical Declassified Intelligence Satellite Photographs back to 1960s, Geophys. Res. Lett., 43(11), 5758-5767, http://doi.org/10.1002/2016GL068990, 2016.

Wulder, M. A., Loveland, T. R., Roy, D. P., Crawford, C. J., Masek, J. G., Woodcock, C. E., Allen, R. G., Anderson, M. C., Belward, A. S., Cohen, W. B., Dwyer, J., Erb, A., Gao, F., Griffiths, P., Helder, D., Hermosillo, T., Hipple, J. D., Hostert, P., Hughes, M. J., Huntington, J., Johnson, D. M., Kennedy, R., Kilic, A., Li, Z., Lymburner, L., McCorkel, J., Pahlevan, N., Scambos, T. A., Schaaf, C., Schott, J. R., Sheng, Y., Storey, J., Vermote, E., Vogelmann, J., White, J. C., Wynne, R. H., and Zhu, Z.: Current status of Landsat program, science, and applications, Remote Sens. Environ., 225(127-147, http://doi.org/10.1016/j.rse.2019.02.015, 2019.

Ye, W., Qiao, G., Kong, F., Ma, X., Tong, X., and Li, R.: Improved geometric modeling of 1960s KH-5 ARGON satellite images for regional antarctica applications, Photogramm. Eng. Rem. S., 83(7), 477-491,2017.

Zhou, C., Zhou, Y., Deng, F., Ai, S., Wang, Z., and E, D.: Seasonal and interannual ice velocity changes of Polar Record Glacier, East Antarctica, Ann. Glaciol., 55(66), 45-51, http://doi.org/10.3189/2014AoG66A185, 2014.

https://doi.org/10.5194/tc-2021-183
Preprint. Discussion started: 17 August 2021

The Cryosphere Discussions
Open Access
EGU

Appendix

Table A1. Information for the Landsat 8 images used for velocity mapping in Experiment 1.

Acquisition date (UTC)	Scene ID
2013/12/03	LC08_L1GT_102107_20131203_20170428_01_T2_B8
2014/11/13	LC08_L1GT_101107_20141113_20170417_01_T2_B8
2015/12/25	LC08_L1GT_102107_20151225_20170331_01_T2_B8
2016/11/25	LC08_L1GT_102107_20161125_20170317_01_T2_B8
2017/11/05	LC08_L1GT_101107_20171105_20171120_01_T2_B8
2018/12/17	LC08_L1GT_102107_20181217_20181227_01_T2_B8
2019/12/29	LC08_L1GT_101107_20191229_20200111_01_T2_B8
2020/10/19	LC08_L1GT_102107_20201019_20201019_01_RT_B8

520

Table A2. Acceleration estimates using least squares regression a and simple average $\overline{a}$ applied to L-velocities of 7-year U' and 1-year U.

Area j	$a\,(U'^{j}_{2013-i})$ (m a^{-2})	$\overline{a}\,(U'^{j}_{2013,2020})$ (m a^{-2})	Diff$(a-\overline{a})$ (m a^{-2})	$a\,(U^{j}_{2013-i})$ (m a^{-2})	$\overline{a}\,(U^{j}_{2013,2020})$ (m a^{-2})	Diff$(a-\overline{a})$ (m a^{-2})
1	4.1	3.4	0.7	4.9	4.6	0.3
2	1.8	1.6	0.2	0.7	0.4	0.3
3	4.4	3.6	0.8	6.6	5.7	0.9
4	4.6	3.4	1.2	5.3	3.9	1.4
5	5.1	4.5	0.6	7.1	6.0	1.1
MEAN	4.0	3.3	0.7	4.9	4.1	0.8
STD	1.3	1.1	0.4	2.5	2.2	0.5

525

Table A3. Information for the Landsat images used for velocity mapping in Experiment 2.

Satellite	Acquisition date (UTC)	Scene ID
Landsat 1 (MSS)	1972/11/28	LM10641121972333AAA04
	1972/11/28	LM10641131972333AAA04

https://doi.org/10.5194/tc-2021-183
Preprint. Discussion started: 17 August 2021

1972/11/28	LM10651121972333FAK04
1972/12/1	LM10671121972336AAA04
1972/12/1	LM10671131972336AAA04
1972/12/2	LM10681121972337AAA04
1972/12/5	LM10711121972340AAA02
1972/12/11	LM10781131972346FAK03
1973/1/2	LM10641141973002AAA04
1973/1/3	LM10831131973003AAA04
1973/1/16	LM10611151973016AAA04
1973/1/17	LM10781141973017XXX01
1973/1/25	LM10681131973025FAK03
1973/1/31	LM10741121973031FAK03
1973/1/31	LM10741131973031FAK03
1973/1/31	LM10741151973031FAK03
1973/2/6	LM10801151973037AAA05
1973/2/8	LM10641151973039AAA02
1973/2/9	LM10831141973040XXX01
1973/2/11	LM10671161973042FAK07
1973/2/12	LM10861121973043FAK03
1973/2/14	LM10701121973045AAA05
1973/2/14	LM10701131973045AAA05
1973/2/20	LM10761121973051FAK03
1973/2/28	LM10661141973059AAA04
1973/2/28	LM10661161973059AAA04
1973/3/6	LM10721131973065XXX01
1973/10/29	LM10751121973302AAA02
1973/10/29	LM10751131973302AAA02
1973/11/4	LM10811131973308FAK03
1973/11/4	LM10811141973308FAK03
1973/11/7	LM10841141973311FAK03
1973/11/21	LM10801131973325FAK03
1973/11/24	LM10641161973328AAA04
1973/12/20	LM10731151973354FAK03
1973/12/25	LM10601161973359AAA04
1973/12/31	LM10661141973365AAA04
1973/12/31	LM10661161973365FAK02
1973/12/31	LM10671141973365FAK02
1973/12/31	LM10671151973365FAK01
1974/1/5	LM10711121974005AAA04
1974/1/5	LM10711131974005AAA04
1974/1/12	LM10781141974012AAA04
1974/1/12	LM10781151974012AAA04

https://doi.org/10.5194/tc-2021-183
Preprint. Discussion started: 17 August 2021

	1974/1/14	LM10621161974014AAA04
	1974/1/16	LM10641141974016AAA02
	1974/1/18	LM10661151974018AAA04
	1974/1/20	LM10861121974020AAA04
	1974/1/25	LM10731121974025AAA05
Landsat 4 (TM)	1988/12/15	LT40601141988350XXX04
	1988/12/15	LT40601151988350XXX03
	1989/1/29	LT40551161989029XXX04
	1989/3/24	LT40651131989083XXX01
	1989/3/24	LT40651141989083XXX11
	1989/3/24	LT40651151989083XXX01
	1989/11/12	LT40641151989316XXX01
	1989/11/14	LT40621121989318XXX02
	1989/11/14	LT40621131989318XXX02
	1989/11/26	LT40661121989330XXX01
	1989/11/30	LT40621151989334XXX01
	1989/12/5	LT40651121989339XXX02
	1989/12/16	LT40621141989350XXX02
Landsat 5 (TM)	1986/1/4	LT50561161986004XXX04
	1986/12/13	LT50571161986347XXX05

530